Alcanivorax borkumensis Biofilms Enhance Oil Degradation By Interfacial Tubulation

ONE SENTENCE SUMMARY

A. borkumensis adapt their interfacial properties over time to evolve their biofilm phenotype and increase their oil consumption

AUTHORS

M. Prasad[1], N. Obana[2,3], S.-Z. Lin[4], K. Sakai[5,6], C. Blanch-Mercader[7], J. Prost[7,8], N. Nomura[1,3], J.-F. Rupprecht[4*], J. Fattaccioli[5,6*], A. S. Utada[1,3*]

AFFILIATIONS

[1]Faculty of Life and Environmental Sciences, University of Tsukuba, 1-1-1 Tennodai, Tsukuba, Ibaraki 305-8572, Japan
[2]Transborder Science Research Center, Faculty of Medicine, University of Tsukuba, 1-1-1 Tennodai, Tsukuba, Ibaraki 305-8575, Japan
[3]Microbiology Research Center for Sustainability (MiCS), University of Tsukuba, 1-1-1 Tennodai, Tsukuba, TARA center, Ibaraki 305-8572, Japan
[4]Aix Marseille Université, Université de Toulon, CNRS, Centre de Physique Théorique, Turing Center for Living Systems, Marseille, France
[5]PASTEUR, Département de Chimie, École Normale Supérieure, PSL Université, Sorbonne Université, CNRS, 75005 Paris, France
[6]Institut Pierre-Gilles de Gennes pour la Microfluidique, 75005 Paris, France
[7]Laboratoire Physico-Chimie Curie UMR168, Institut Curie, Paris Sciences et Lettres, Centre National de la Recherche Scientifique, Sorbonne Université, 75248 Paris, France
[8]Mechanobiology Institute, National University of Singapore, 117411 Singapore

Correspondence: utada.andrew.gm@u.tsukuba.ac.jp, jacques.fattaccioli@ens.psl.eu, jean-francois.rupprecht@univ-amu.fr

ABSTRACT

Alcanivorax borkumensis are prominent actors in oil spill bioremediation; however, the interfacial dynamics of their biofilms and its role in oil degradation remain unclear. Longitudinal tracking of bacteria-covered oil droplets using microfluidics, reveals distinct biofilm phenotypes: thick and spherical versus thin and dendritic, with the latter having a faster consumption rate. We show experimentally that biofilm dendrites emerge from aster-like nematic defects in thin biofilms. We develop a theoretical model that elucidates the transition between phenotypes; this model links tubulation to decreased interfacial tension and increased cell hydrophobicity, which we verify experimentally. *A. borkumensis* manipulates its interfacial properties to utilize division to drive an increase in surface area, which could be the cause for its rapid blooming and dominance after oil spills.

KEYWORDS

Alcanivorax borkumensis; Oil bioremediation; Microfluidics, Confined Nematic Ordering, Collective Behavior; Contact angle; Cell-surface Hydrophobicity

INTRODUCTION

Obligately hydrocarbonoclastic bacteria (OHCB) are a group of cosmopolitan marine bacteria with an unusual ecology: they can survive by consuming hydrocarbons as a sole energy and carbon source (*1*). In the marine environment, these bacteria are typically found at very low densities but can bloom to become the dominant bacteria at the site of oil spills (*1*, *2*). They are thought to degrade a significant amount of the worldwide spilled oil (*3*–*5*), which has generated interest in these organisms for their technological potential as agents of bioremediation (*5*–*8*).

Alcanivorax borkumensis SK2 (*9*) was the first hydrocarbonoclastic bacteria whose genome was sequenced and is frequently used as a model OHCB (*6*). Like most bacteria, it transitions between a free-living lifestyle to one as part of a social collective, called a biofilm, which is now recognized as integral to bacterial biology (*11*, *12*). Most biofilms are 3-dimensional communities of densely packed cells that cooperatively secrete extracellular polymeric substances (EPS) that both protect and help the community remain attached to solid surfaces (*10*). This high cell density creates gradients where outward-facing cells have greater access to important nutrients than cells in the interior. However, unlike most biofilm-forming bacteria, *A. borkumensis* form biofilms at the oil-water, a liquid-liquid interface; here, the formation of biofilm creates opposing gradients in the access to oil relative to nutrients needed for respiration. How these nutritive gradients and the fluid nature of the interface affects OHCB biofilm formation and oil consumption remains largely unexplored.

Most knowledge of bacteria-mediated oil degradation comes from metagenomic assays (*6*, *13*), mutant screens (*14*), interfacial rheology (*15*–*18*), and microcosm tests (*19*–*21*). However, a comprehensive picture of the mechanism of biofilm formation and its coupling to oil degradation remains unclear. To date, few studies have focused on the dynamics of OHCB biofilms formation at the oil/water interface at the micro-drop scale (*22*–*24*). Nonetheless, these studies do not resolve the physical process of biofilm formation and oil degradation at the single bacterium scale.

To address these questions, we developed a microfluidic device that allows the trapping and real-time imaging of numerous bacteria-covered oil droplets; this platform allows us to capture the full dynamics of biofilm development starting from individual bacteria through the complete

consumption of oil droplets. We show that *A. borkumensis* presents distinct biofilm phenotypes that correlate with culture time using oil. For short culture times, they present as a thick, spherical biofilm (SB) that envelops the droplet. For long culture times, they present as a thin, dendritic biofilm (DB) that stretches and tubulates the drop interface, leading to rapid consumption. We show that tubulation is initiated at aster-like topological defects found in the nematic order of interfacial cells. Using a coarse grain model to describe the biofilm dynamics, we predict that the balance between cell density, interfacial tension, and cell hydrophobicity facilitates exponential stretching of the interface and confirm this experimentally. Ultimately, the capacity to generate tubulation at the oil-water interface could be the cause for the blooming and dominance of *A. borkumensis* after oil spills.

RESULTS

Experimental setup and microfluidic device

In pristine marine environments, *A. borkumensis* primarily uses water soluble organic acids, such as pyruvate, as its carbon and energy source. During marine oil spills, they transition to using water-insoluble alkanes. To study the biofilm dynamics after this transition, we initially cultivate the bacteria using pyruvate, and then switch to a minimal medium supplemented with hexadecane (C16), where we incubate up to 5 days (d) (**Fig. S1A** and **Supplementary Information (SI) - Methods** section). Using these cultures, periodically sample the bacteria by generating cell-laden oil microdroplets with fresh C16, which we store in individual traps in our microfluidic platform (*25*). This device facilitates *in situ* culturing, which then enables the longitudinal investigation of biofilm development on specific droplets (**Fig. 1A**, **Fig. S2A,** and **SI - Microfluidics**). Drops imaged immediately after being trapped initially have ~20-50 cells attached (**Fig. S3A**). These cells divide to form a confluent monolayer over the course of ~12 h. We define the t_0 of our experiments as the moment of confluency.

Bacteria exhibit two distinct phenotypes and consumption rates

Sampling bacteria over 5 d reveals different phenotypes that manifest vastly different biofilm morphologies and oil consumption rates. When sampled after 1 d, *A. borkumensis* form a spherical biofilm (SB) that grows radially outward from the oil; here, the oil droplet remains spherical as it is consumed **(Fig. 1B, Fig. S3B, and Movie S1)**. In striking contrast, bacteria sampled from 5 d culture can form monolayer-thin biofilms with a local nematic ordering of the bacteria on the droplet surface that buckles and then tubulates the interface, as shown in the 0-16 h sequence in **Fig. 1C**; we call these dendritic biofilms (DB). In this case, the magnitude of the deformations grow as the oil is consumed; this process ultimately shreds the droplets into tiny fragments (**Fig. S3C and Movie S2)**.

We quantify the oil consumption rate for each phenotype by measuring the droplet volume (V) from brightfield and confocal images of the droplet surface area (S) over time (**SI - Methods**). SBs consume >90% of the initial volume in ~72 h, whereas DBs achieve the same in ~20 h. We find that the oil volume of SBs decreases as a polynomial function of time, whereas for DBs, the decay is much faster (**SI - Eq.11**). In both cases, this decrease is consistent with a model that assumes that only interfacial bacteria consume oil (**Fig. 1D,E and SI - Analytical Model of Oil Consumption**).

The good agreement between our analytical models and data allows us to estimate the per-cell consumption rates of both SB and DB cells as 0.7 and 0.8 fL/h, respectively; this small difference in consumption rate is consistent with their similar division times (**Fig. S1D**). For comparison, the volume of a single cell is ~1 fL, meaning that these bacteria consume a volume of oil close to their own, every hour. Despite the similarity in consumption rates on a per cell basis, the normalized surface-to-volume ratio (S^*/V^*) shows that DBs are significantly more efficient: S^*/V^* doubles in 72 h for SBs, whereas it diverges in less than 24 h for DBs (**Fig. 1E, inset**). The S^*/V^* ratio provides a means for comparing the relative efficiencies of the two phenotypes and highlights the fact that these differences arise from the rapid increase in S caused by DB biofilms. In both cases, the shape of the interface defines the dynamics of volume decrease. For SBs, the interfacial area set by the spherical droplet determines the number of cells (N) that can pack onto the interface to have access to the oil. Conversely, the exponential increase of N due to cell division for DBs determines the interfacial area. Thus, the rate of consumption decreases over time for SBs, while the rate continuously increases for DBs.

Tubulation is facilitated by topological defects

We correlate the onset of the exponential surface area increase in DBs to the emergence of nematic order of the interfacial cells. Numerous examples have shown that rod-like bacteria can locally align in the same direction, defining a nematic order field (*26*–*31*). Active systems with nematic order have demonstrated the ability, both in theory (*32*) and in experiments (*33*–*36*), to utilize topological defects to achieve surface deformation. Here, at 2-4 h post-confluency, we observe the appearance of conical protrusions composed of cells originating at the core of aster-like topological defects within the nematic field (**Fig. 2A,B** and **Fig. S4)**. As the biofilm matures, more protrusions appear while existing protrusions develop into branched bacteria-covered tubes (**Fig. 1C (16 h)** and **Fig. 2C)**.

Differential labeling of the oil and cells reveals that the tubes are not hollow but rather filled with oil (**Fig. S5A**); this result indicates that cell adhesion at the interface stabilizes the tubes against collapse and thereby prevents the droplet from returning to a sphere. Furthermore, a careful

inspection of the confocal images of the tubes reveals that the bacteria are well aligned to the tube axis. To characterize this alignment, we generate the orientation director field of the cells on the tube (**Fig. 2D**). We then estimate cell alignment along the tube by determining the average scalar product between the director field and the tube axis direction. Our calculated values along the tube are all close to 1, indicating that the cells are highly aligned with the tube axis (**Fig. 2E, Fig. S5B and C,** and **SI - Methods**).

Due to this parallel alignment of cells on the tubes, we hypothesize that the rate of tube-length increase is proportional to the number of cells on the tube, which should increase exponentially. We measure tube elongation, finding that it increases exponentially, confirming our hypothesis (**Fig. 2F**, **Fig. S5D**, and **SI-Methods**). From the exponential fit, we extract a tube length-doubling time of ~3.4 h, which is about twice the cell division time (t_{div}) of 1.65 h (**Fig. S1D**). This difference arises from the fact that cell alignment is close to but not equal to 1 and because some number of cells are displaced from the interface, which are visible around the tubes (**Fig. 2C**).

Biofilm phenotypes are associated with a decrease of interfacial tension

The vastly different surface morphologies of the two biofilm phenotypes suggest differences in their interfacial properties. *A. borkumensis* secrete biosurfactants both on the cell surface and into the environment, which are thought to aid in oil assimilation (*37*, *38*). These biosurfactants can lower the oil-water interfacial tension (γ) and form conditioning films at interfaces that facilitate surface colonization. To measure differences in interfacial properties based on biofilm phenotype, we fractionate SB and DB cultures into three components: cells, conditioned media, and conditioned C16 to independently measure γ for each (**Fig. S6A**). We find that all of the respective fractions show depressed values of γ relative to control values; however, the DB-conditioned oil decreases the most. The γ for DB-conditioned oil decreases from 30 to 8 mN/m and is about half the value for SBs (**Fig. 3A, Fig. S6B-D** and **Table S1**). Microfluidic “re-sampling” of biofilm phenotype using the DB-conditioned C16 instead of fresh oil, surprisingly reveals no change in observed phenotype (**Fig. S6E**). Thus, despite the ~4 fold lower γ of DB-conditioned oil, the SB cells are unable to deform the oil-water interface, indicating that a lower γ is not sufficient to produce the DB phenotype.

Interfacial behavior is also affected by cell hydrophobicity, which, together with γ controls the extent to which cells are wetted by the oil (**Fig. S7A**). Cell hydrophobicity is thought to increase the longer cells consume oil, however the relationship with phenotype is unclear (*21*, *39*). Although the bacteria appear to lay flat on the surface at t_0, the microscopic contact angle is difficult to estimate from confocal images (**Fig. S7B)**. Thus, to estimate hydrophobicity for the cells of both phenotypes, we measure the 3-phase contact angle (θ) between water that we deposit on a bacterial lawn

submerged in oil (*40*) (**Fig. S7C-E** and **SI - Methods**); larger θ's indicate larger hydrophobicity and θ=90° is the neutral wetting condition. SB cells, which are isolated after 1 d of culture, have θ≈80°, whereas DB cells, which are isolated after 5 d, have a θ≈100° (**Fig. 3B** and **SI - Methods**). This indicates that the midplanes of SB and DB cells are ±10% above and below the interface, respectively (**Fig. S7A**).

The higher hydrophobicity of DB cells indicates that they have a larger interfacial adhesion strength than SB cells. To directly compare the respective adhesion strengths of SB and DB, we force them to compete for interfacial area on oil microdroplets, noting that both phenotypes have similar division times (**Fig. S1D**). We generate cell-laden droplets using mCherry-expressing SB cells and GFP-expressing DB cells in a 3:1 ratio, and record fluorescence intensity as the biofilm develops. Since the same oil substrate is used, we ensure that both phenotypes experience the same γ. We find that although the DB cells are initially in the minority, they gradually displace the established SB, to become dominant in ~5 h (**Fig. 3C,D**). This result confirms our expectation that DB cells, which are more hydrophobic do indeed have a larger adhesion energy to the interface than SB cells.

Rod-shaped gammaproteobacteria like *Pseudomonas aeruginosa* have been shown to colonize and remodel oil-water interfaces with their biofilms, similar to what we observe in the early stages (<3 h) of DB formation (*17*, *18*, *41*). However, those biofilms lack the large-scale deformations that we observe in later stages (**Fig. 1C**, >5 h). From our measurement of the oil-water interfacial tension, we estimate that the biofilm compression modulus is ~200 Pa (*42*), which is much smaller than the estimated ~1 MPa extensional growth pressure of *P. aeruginosa* (*43*). Assuming that *A. borkumensis* have a similar growth pressure, cell division supplies enough stress to easily deform the interface. Thus, DBs generate the biofilm phenotypes we observe only if a sufficient number of cells remain adhered to the interface to drive the tubulation process. Conversely, that lack of deformations in the SB phenotype is the consequence of cell-detachment followed by biofilm formation around the interface.

Membrane theory predicts the transition from SB to DB phenotype

Based on these observations, we develop a coarse-grain membrane model to describe the interfacial dynamics of the growing interfacial dendritic biofilm. The model explains the transition between SB and DB phenotypes in terms of a competition between the interfacial tension and the spontaneous curvature of the cell-laden interface. As the biofilm deforms the droplet, it works against interfacial tension to expand the surface. Simultaneously, the spontaneous curvature, which describes the intrinsic tendency of the biofilm to bend in a preferred direction, governs the shape of the expanding surface. The resultant shape is a tube when the energetic cost of increasing surface area is lower than the cost of bending. This results in an exponential tube expansion rate:

$$\frac{\dot{L}}{L} = \left(\frac{\kappa_B}{2r_0^2} - \gamma\right)/\eta \quad \text{Eq. (1)}$$

where L is the tube length, κ_B is the bending rigidity of the membrane in the circumferential direction of the tube, r_0 is the tube radius, $1/r_0$ is the spontaneous curvature of the biofilm, and η is the viscosity of the biofilm (**Supplementary Information** and **Fig. S14**).

Eq. 1 can be generalized to encompass active extensile nematic stresses driven by bacterial growth, with γ being replaced by an effective interfacial tension $\gamma_{eff}(\varrho)$ that depends on the interfacial cell density ϱ (**Supplementary Information**). This implies that tubulation occurs at a critical density (ϱ_B), which is consistent with the observation that tubes form after confluency (**Fig. 1C**). Conversely, lowering ϱ by removing the bacteria would allow the recovery of the spherical shape. To test this hypothesis, we generate DBs and then expose them to a flowing surfactant mixture to disrupt the biofilm (**SI - Methods**). Following a ~4 h lag, the biofilm abruptly washes away, allowing the deformed droplets to become spherical (**Fig. S8A,B** and **Movie S3**); this is the consequence of positive interfacial tension in the absence of bacteria.

In addition to the SB and DB phenotypes described so far, we observe an intermediate phenotype when we isolate cells at an intermediate culture time (**Fig. S1A**). These biofilms present dynamic oscillatory behavior (OB), alternating between the dendritic and spherical biofilms, with a period of ~12 h (**Fig. 3E**, **Fig. S9,** and **Movie S5**). The relatively short (~30 min) transition from tubulated back to spherical is consistent with a sudden loss of tube stability, which, based on **Eq. 1**, is consistent with a sudden increase in the effective surface tension.

To elucidate the emergence of oscillations between spherical and dendritic phenotypes, we use a phase-field approach following an established literature on simulating interfacial dynamics of multiphasic systems (*44*). Here the simulated field is the local fraction of oil (φ(x,y)) that obeys a Cahn-Hilliard equation with an interfacial term $\kappa_1(\rho)(\nabla\varphi)^2/2$, where $\kappa_1(\rho)$ is the mechanical work needed to expand the biofilm surface area, which sets the tube expansion rate, as described in **Eq. 1** (**Supplementary Information**). Prior to confluency, while the interfacial cell density is low, we define $\kappa_1(\rho) = \gamma - k_1 \rho$, where k_1 accounts for the force applied by the biofilm to deform the oil. Tubulation occurs when $\kappa_1(\rho)<0$, which sets a critical cell density where the interface buckles (ρ_B). The interface remains spherical when $\kappa_1(\rho)>0$, where the density is lower than the critical buckling density (**Fig. 3F**). Starting from a circular oil-water interface modeled with a low bacterial density at t_0, the cell density grows logistically towards a homeostatic density (ρ_H), where cell division and loss from the interface are balanced (**Movie S4**). The homeostatic density determines the observed phenotype: when $\rho_H < \rho_B$, tubes are unable to form, resulting in the SB phenotype (**Fig. 3F,**

magenta); when $\rho_H > \rho_B$, stable tubes form, producing the DB phenotype (**Fig. 3F, green**). The emergence of oscillations can be then understood in terms of a saturation mechanism (ρ^2 term) in the rate of tube expansion $\kappa_1(\rho)$, such that it displays a minimum at an optimal cell density denoted ρ_S (**Fig. 3F**). At this optimal density, both the tube length expansion and final tube length are maximal (**Supplementary Information**). Oscillations arise for a specific range of parameters $\rho_H > \rho_S > \rho_B$ (**Fig. 3F, blue and Supplementary Information**). In this regime, as the cell density (ρ) increases beyond the optimal value ρ_S to reach ρ_H, the tube length no longer lengthens but instead contracts. During contraction, the bacterial density further increases due to the loss in surface area; this leads ρ to overshoot ρ_H, causing $\kappa_1(\rho) > 0$ at high density. This overshoot ultimately induces the catastrophic collapse of the tube structures and a large reduction in the number of adhered bacteria. Consistent with this prediction, we observe in experiments large and persistent flows of cells away from the interface soon after tube collapse (**Movie S5**). Our biomechanical model recapitulates the transition from these three phenotypes in terms of a tubulation mechanism that depends on the bacterial growth dynamics, with oscillations emerging through a dynamical phase transition mechanism (*45*) (**Fig. 3G, Movie S4**). These oscillations are driven by continuous cell division that drives a density increase beyond critical values for tube growth and collapse.

Confined droplets buckle from disclinations

We leverage microfluidics to position the defects that generate tubes by controlling the shape of trapped drops. Droplets whose diameters are smaller than the trap height remain spherical in the pocket; droplets whose diameters are larger than the trap height are flattened into pancakes (**Fig. 4A - Upper inset)**. We use these flat circular zones at the top and bottom of the drops to control the location of the defects, which enables us to concentrate growth stress in the center; this focusing consistently generates dimples at the same location. Initially, interfacial surface tension excludes bacteria from the flattened regions (**Fig. 4A** and **Fig. S10(A-B)**). In time, growth pressure drives the cells into the flat circular zones, generating a confluent monolayer with an aster-like +1 defect (or two closely spaced +1/2 defects) in the center (**Fig. 4B, Fig. S10(C-D)**, and **Movie S6**) (*46*, *47*). As cell division continues, we observe the formation of a large dimple at the defect, which grows inward into the droplet (**Fig. 4C** and **Fig. S10E)**. A similar process occurs at the top of the drop by symmetry (**Fig. S10B-inset**). We find that the height profile of the dimple agrees with a model of spontaneous deformation of a liquid crystalline membrane with a radial nematic order (**SI - Fitting Procedure Dimple Profile**) (*48*, *49*), given by:

$$h = h_0 \int_R^r K\left(\sqrt{1-\frac{\kappa_F}{\kappa_B}}, \frac{r'}{\sqrt{\kappa_B/\gamma}}\right) dr' \quad \text{(Eq. 2)}$$

where *h* is the dimple height, *K(α,x)* is a modified Bessel function of order α, and κ_F is the elastic constant of the nematic director field. The rounded shape at the inward tip is a consequence of the finite size of the bacteria with non-zero bending moduli.

DISCUSSION

We use a microfluidic platform that allows us to trap, culture, and image cell-laden oil drops with unprecedented spatial and temporal resolution. Our work stands in contrast with most studies to date, which obtain average measurements from bulk methods. Sampling *A. borkumensis* cells that are adapted to grow using oil over 5 days, we show that at the single-biofilm level, the phenotype is more complex than previously known, possessing the ability for explosive growth. Moreover, *A. borkumensis* effect this transition by modulating their interfacial properties, which enables a dramatic increase in the, per-biofilm, rate of oil consumption. Importantly, this is possible because a subset of exponentially growing cells remain in direct contact with oil as they divide. Their division, thus, drives the exponential stretching of the interface. These features demonstrate the remarkable ability of *A. borkumensis* to manipulate the shape of their food substrate to maximize their collective intake, which is unique for bacteria.

We also explain how buckling and tubulation arise from nematic defects based on the hydrodynamics of rod-shaped objects along curved interfaces. Our theoretical model, built from a minimal set of parameters, predicts the full phase diagram of biofilm phenotypes and further clarifies that the interfacial properties of the bacteria affect the local bending of the interface - and - this is crucial for the formation of tubes.

From the ecological perspective, how *A. borkumensis* outcompetes other oil-consuming organisms after oil spills is still an unsolved problem. The environment and composition of spilled petroleum likely play a role in the selection of the microorganisms that can take advantage of it; however, the tubulation mechanism we describe could be the reason that this species becomes dominant after the sudden appearance of a plentiful but water-insoluble carbon source. Our microfluidic platform is sufficiently general to enable the study of the population dynamics of mixtures of different oil-consuming microorganisms subjected to different substrates, culture conditions, and different oil-dispersants to provide insight into improving current remediation procedures in the field.

CONTRIBUTIONS

MP, NO, KS performed the experiments; MP, CBM, NO, NN, JF, ASU analyzed and discussed the data; CBM, JP, JFR, SZL designed the tubulation theory; SZL carried out simulations; MP, CBM, NO, JFR, JF, ASU wrote the manuscript; JF and ASU conceived of the project.

ACKNOWLEDGMENTS

We thank Y. Yamashita (UT) for use of the contact angle/pendant drop systems, F. Pincet (Laboratoire de Physique, ENS) for assistance with micropipette experiments, D. Quéré (ESPCI) for the fruitful discussion on the O/W/cell contact angle measurements, and F. Brochard-Wyart (Institut Curie) for discussions on tube formation.

FUNDING

The research leading to these results was supported by the JSPS–ANR SAKURA Grant (JF, ASU, NO), JSPS BRIDGE Fellowship (JF), JST-ERATO (NN) (JPMJER1502), JSPS Kakenhi B (ASU) (21H01720), France 2030 (ANR-16-CONV-0001) (JFR), Excellence Initiative of Aix-Marseille University - A*MIDEX (JFR) and ANR-20-CE30-0023 (JFR).

COMPETING INTERESTS

The authors declare that they have no competing interests.

DATA AND MATERIALS AVAILABILITY

All materials are available upon request.

SUPPLEMENTARY MATERIALS

Supplementary Information:

- Materials And Methods,
- Analytical Model Of Oil Consumption
- Extended Tubulation Model
- Fitting Procedure For The Dimple Profiles
- Supplementary Figures : Fig S1 – S17
- Supplementary Tables : Table S1 – S2
- Supplementary Movies : Movie S1-S6

REFERENCES

1. I. M. Head, D. M. Jones, W. F. M. Röling, Marine microorganisms make a meal of oil. *Nat. Rev. Microbiol.* **4**, 173–182 (2006).
2. Y. Kasai, H. Kishira, T. Sasaki, K. Syutsubo, K. Watanabe, S. Harayama, Predominant growth of Alcanivorax strains in oil-contaminated and nutrient-supplemented sea water. *Environ. Microbiol.* **4**, 141–147 (2002).
3. A. Hara, K. Syutsubo, S. Harayama, Alcanivorax which prevails in oil-contaminated seawater exhibits broad substrate specificity for alkane degradation. *Environ. Microbiol.* **5**, 746–753 (2003).
4. W. F. M. Röling, M. G. Milner, D. M. Jones, F. Fratepietro, R. P. J. Swannell, F. Daniel, I. M. Head, Bacterial community dynamics and hydrocarbon degradation during a field-scale evaluation of bioremediation on a mudflat beach contaminated with buried oil. *Appl. Environ. Microbiol.* **70**, 2603–2613 (2004).
5. R. M. Atlas, T. C. Hazen, Oil biodegradation and bioremediation: a tale of the two worst spills in U.S. history. *Environ. Sci. Technol.* **45**, 6709–6715 (2011).
6. S. Schneiker, V. A. P. Martins dos Santos, D. Bartels, T. Bekel, M. Brecht, J. Buhrmester, T. N. Chernikova, R. Denaro, M. Ferrer, C. Gertler, A. Goesmann, O. V. Golyshina, F. Kaminski, A. N. Khachane, S. Lang, B. Linke, A. C. McHardy, F. Meyer, T. Nechitaylo, A. Pühler, P. N. Golyshin, Genome sequence of the ubiquitous hydrocarbon-degrading marine bacterium Alcanivorax borkumensis. *Nat. Biotechnol.* **24**, 997–1004 (2006).
7. T. C. Hazen, E. A. Dubinsky, T. Z. DeSantis, G. L. Andersen, Y. M. Piceno, N. Singh, J. K. Jansson, A. Probst, S. E. Borglin, J. L. Fortney, W. T. Stringfellow, M. Bill, M. E. Conrad, L. M. Tom, K. L. Chavarria, T. R. Alusi, R. Lamendella, D. C. Joyner, C. Spier, J. Baelum, O. U. Mason, Deep-sea oil plume enriches indigenous oil-degrading bacteria. *Science*. **330**, 204–208 (2010).
8. F. Mapelli, A. Scoma, G. Michoud, F. Aulenta, N. Boon, S. Borin, N. Kalogerakis, D. Daffonchio, Biotechnologies for Marine Oil Spill Cleanup: Indissoluble Ties with Microorganisms. *Trends Biotechnol.* **35**, 860–870 (2017).
9. M. M. Yakimov, P. N. Golyshin, S. Lang, E. R. Moore, W. R. Abraham, H. Lünsdorf, K. N. Timmis, Alcanivorax borkumensis gen. nov., sp. nov., a new, hydrocarbon-degrading and surfactant-producing marine bacterium. *Int. J. Syst. Bacteriol.* **48 Pt 2**, 339–348 (1998).
10. R. M. Donlan, Biofilms: microbial life on surfaces. *Emerging Infect. Dis.* **8**, 881–890 (2002).
11. L. Hall-Stoodley, J. W. Costerton, P. Stoodley, Bacterial biofilms: from the natural environment to infectious diseases. *Nat. Rev. Microbiol.* **2**, 95–108 (2004).
12. J. K. Teschler, D. Zamorano-Sánchez, A. S. Utada, C. J. A. Warner, G. C. L. Wong, R. G. Linington, F. H. Yildiz, Living in the matrix: assembly and control of Vibrio cholerae biofilms. *Nat. Rev. Microbiol.* **13**, 255–268 (2015).
13. W. Wang, Z. Shao, Enzymes and genes involved in aerobic alkane degradation. *Front. Microbiol.* **4**, 116 (2013).
14. J. S. Sabirova, T. N. Chernikova, K. N. Timmis, P. N. Golyshin, Niche-specificity factors of a marine oil-degrading bacterium Alcanivorax borkumensis SK2. *FEMS Microbiol. Lett.* **285**,

89–96 (2008).

15. P. A. Rühs, L. Böcker, R. F. Inglis, P. Fischer, Studying bacterial hydrophobicity and biofilm formation at liquid–liquid interfaces through interfacial rheology and pendant drop tensiometry. *Colloids and Surfaces B: Biointerfaces*. **117**, 174–184 (2014).

16. L. Vaccari, M. Molaei, T. H. R. Niepa, D. Lee, R. L. Leheny, K. J. Stebe, Films of bacteria at interfaces. *Adv. Colloid Interface Sci.* **247**, 561–572 (2017).

17. T. H. R. Niepa, L. Vaccari, R. L. Leheny, M. Goulian, D. Lee, K. J. Stebe, Films of Bacteria at Interfaces (FBI): Remodeling of Fluid Interfaces by Pseudomonas aeruginosa (vol 7, 17864, 2017). *Scientific Reports*. **9** (2019).

18. G. Subbiahdoss, E. Reimhult, Biofilm formation at oil-water interfaces is not a simple function of bacterial hydrophobicity. *Colloids Surf. B Biointerfaces*. **194**, 111163 (2020).

19. L. G. Whyte, S. J. Slagman, F. Pietrantonio, L. Bourbonnière, S. F. Koval, J. R. Lawrence, W. E. Inniss, C. W. Greer, Physiological adaptations involved in alkane assimilation at a low temperature by Rhodococcus sp. strain Q15. *Appl. Environ. Microbiol.* **65**, 2961–2968 (1999).

20. R. Grimaud, in *Handbook of hydrocarbon and lipid microbiology*, K. N. Timmis, Ed. (Springer Berlin Heidelberg, Berlin, Heidelberg, 2010), pp. 1491–1499.

21. M. P. Godfrin, M. Sihlabela, A. Bose, A. Tripathi, Behavior of marine bacteria in clean environment and oil spill conditions. *Langmuir*. **34**, 9047–9053 (2018).

22. C. Joannis-Cassan, M. Delia, J. Riba, Limitation phenomena induced by biofilm formation during hydrocarbon biodegradation. *Journal of Chemical Technology and Biotechnology*. **80**, 99–106 (2005).

23. N. K. Dewangan, J. C. Conrad, Adhesion of Marinobacter hydrocarbonoclasticus to Surfactant-Decorated Dodecane Droplets. *Langmuir*. **34**, 14012–14021 (2018).

24. V. Hickl, G. Juarez, Tubulation and dispersion of oil by bacterial growth on droplets. *Arxiv* (2022) (available at https://doi.org/10.48550/arXiv.2207.02285).

25. R. Dangla, S. Lee, C. N. Baroud, Trapping microfluidic drops in wells of surface energy. *Phys. Rev. Lett.* **107**, 124501 (2011).

26. F. Beroz, J. Yan, B. Sabass, H. A. Stone, B. L. Bassler, N. S. Wingreen, Y. Meir, Verticalization of bacterial biofilms. *Nat. Phys.* **14**, 954–960 (2018).

27. K. Drescher, J. Dunkel, C. D. Nadell, S. van Teeffelen, I. Grnja, N. S. Wingreen, H. A. Stone, B. L. Bassler, Architectural transitions in Vibrio cholerae biofilms at single-cell resolution. *Proc Natl Acad Sci USA*. **113**, E2066-72 (2016).

28. O. J. Meacock, A. Doostmohammadi, K. R. Foster, J. M. Yeomans, W. M. Durham, Bacteria solve the problem of crowding by moving slowly. *Nat. Phys.* (2020), doi:10.1038/s41567-020-01070-6.

29. J. Nijjer, C. Li, Q. Zhang, H. Lu, S. Zhang, J. Yan, Mechanical forces drive a reorientation cascade leading to biofilm self-patterning. *Nat. Commun.* **12**, 6632 (2021).

30. K. Copenhagen, R. Alert, N. S. Wingreen, J. W. Shaevitz, Topological defects promote layer formation in *Myxococcus xanthus* colonies. *Nat. Phys.* (2020), doi:10.1038/s41567-020-01056-4.

31. B. Qin, C. Fei, A. A. Bridges, A. A. Mashruwala, H. A. Stone, N. S. Wingreen, B. L. Bassler,

Cell position fates and collective fountain flow in bacterial biofilms revealed by light-sheet microscopy. *Science*. **369**, 71–77 (2020).

32. L. Metselaar, J. M. Yeomans, A. Doostmohammadi, Topology and Morphology of Self-Deforming Active Shells. *Physical Review Letters*. **123** (2019).

33. K. Kawaguchi, R. Kageyama, M. Sano, Topological defects control collective dynamics in neural progenitor cell cultures. *Nature*. **545**, 327–331 (2017).

34. P. Guillamat, C. Blanch-Mercader, G. Pernollet, K. Kruse, A. Roux, Integer topological defects organize stresses driving tissue morphogenesis. *Nat. Mater.* **21**, 588–597 (2022).

35. Y. Maroudas-Sacks, L. Garion, L. Shani-Zerbib, A. Livshits, E. Braun, K. Keren, Topological defects in the nematic order of actin fibres as organization centres of Hydra morphogenesis. *Nat. Phys.* **17**, 251–259 (2021).

36. T. B. Saw, A. Doostmohammadi, V. Nier, L. Kocgozlu, S. Thampi, Y. Toyama, P. Marcq, C. T. Lim, J. M. Yeomans, B. Ladoux, Topological defects in epithelia govern cell death and extrusion. *Nature*. **544**, 212–216 (2017).

37. M. P. Kem, H. K. Zane, S. D. Springer, J. M. Gauglitz, A. Butler, Amphiphilic siderophore production by oil-associating microbes. *Metallomics*. **6**, 1150–1155 (2014).

38. A. Passeri, M. Schmidt, T. Haffner, V. Wray, S. Lang, F. Wagner, Marine biosurfactants. IV. Production, characterization and biosynthesis of an anionic glucose lipid from the marine bacterial strain MM1. *Applied Microbiology and Biotechnology*. **37**, 281–286 (1992).

39. N. L. Olivera, M. L. Nievas, M. Lozada, G. Del Prado, H. M. Dionisi, F. Siñeriz, Isolation and characterization of biosurfactant-producing Alcanivorax strains: hydrocarbon accession strategies and alkane hydroxylase gene analysis. *Res. Microbiol.* **160**, 19–26 (2009).

40. L. S. Dorobantu, A. K. C. Yeung, J. M. Foght, M. R. Gray, Stabilization of oil-water emulsions by hydrophobic bacteria. *Appl. Environ. Microbiol.* **70**, 6333–6336 (2004).

41. L. Vaccari, D. B. Allan, N. Sharifi-Mood, A. R. Singh, R. L. Leheny, K. J. Stebe, Films of bacteria at interfaces: three stages of behaviour. *Soft Matter*. **11**, 6062–6074 (2015).

42. D. Vella, P. Aussillous, L. Mahadevan, Elasticity of an interfacial particle raft. *Europhysics Letters*. **68**, 212–218 (2004).

43. H. H. Tuson, G. K. Auer, L. D. Renner, M. Hasebe, C. Tropini, M. Salick, W. C. Crone, A. Gopinathan, K. C. Huang, D. B. Weibel, Measuring the stiffness of bacterial cells from growth rates in hydrogels of tunable elasticity. *Mol. Microbiol.* **84**, 874–891 (2012).

44. J. W. Cahn, Phase separation by spinodal decomposition in isotropic systems. *J. Chem. Phys.* **42**, 93–99 (1965).

45. F. Jülicher, A. Ajdari, J. Prost, Modeling molecular motors. *Rev. Mod. Phys.* **69**, 1269–1282 (1997).

46. G. Salbreux, J. Prost, J. F. Joanny, Hydrodynamics of cellular cortical flows and the formation of contractile rings. *Phys. Rev. Lett.* **103**, 058102 (2009).

47. P. G. de Gennes, J. Prost, *The Physics Of Liquid Crystals (International Series Of Monographs On Physics)* (Oxford University Press, U.S.A., ed. 2, 1995).

48. J. R. Frank, M. Kardar, Defects in nematic membranes can buckle into pseudospheres. *Physical Review E*. **77**, 041705 (2008).

49. L. A. Hoffmann, L. N. Carenza, J. Eckert, L. Giomi, Theory of defect-mediated morphogenesis. *Sci. Adv.* **8**, eabk2712 (2022).

FIGURES

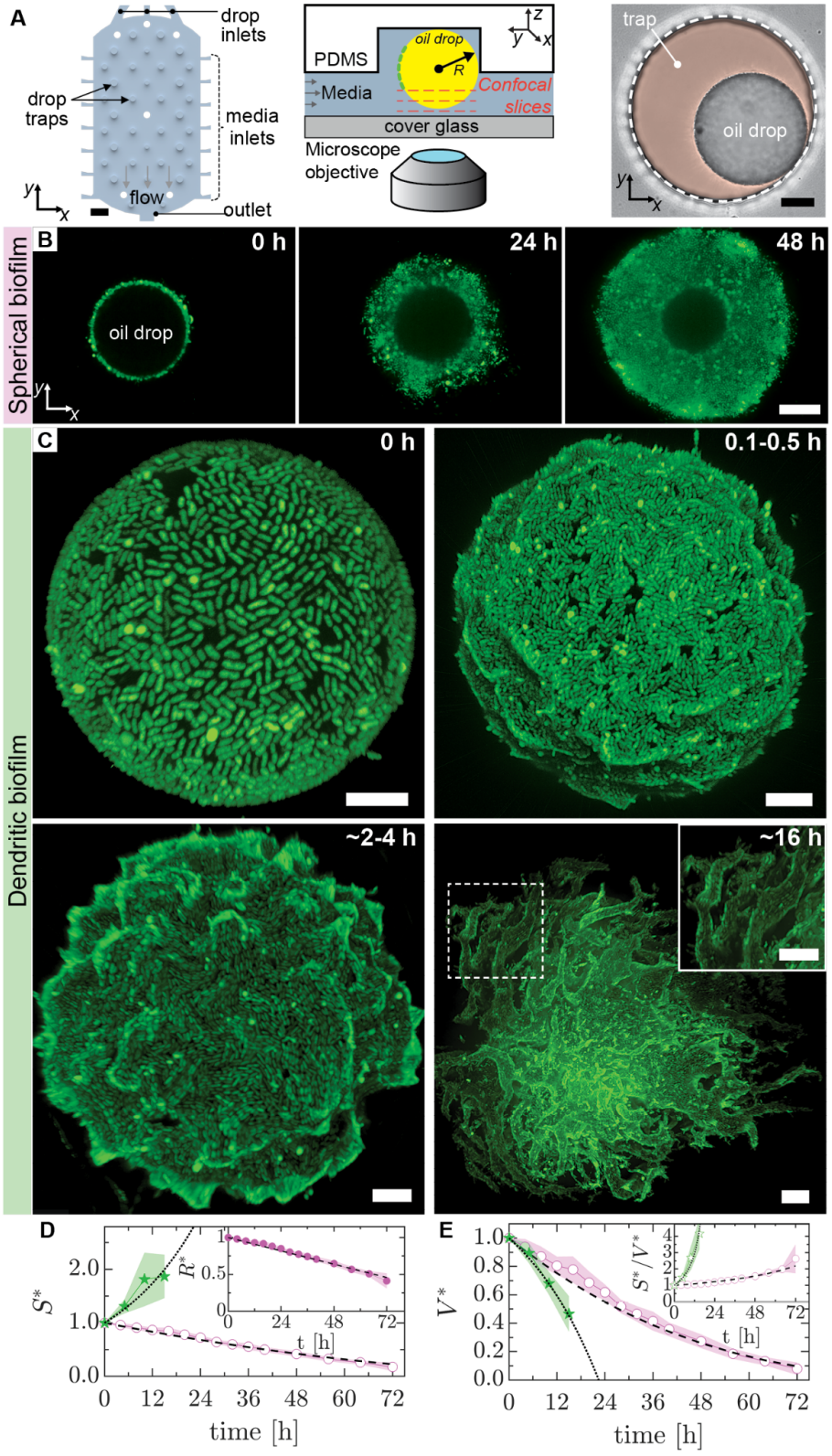

Fig. 1

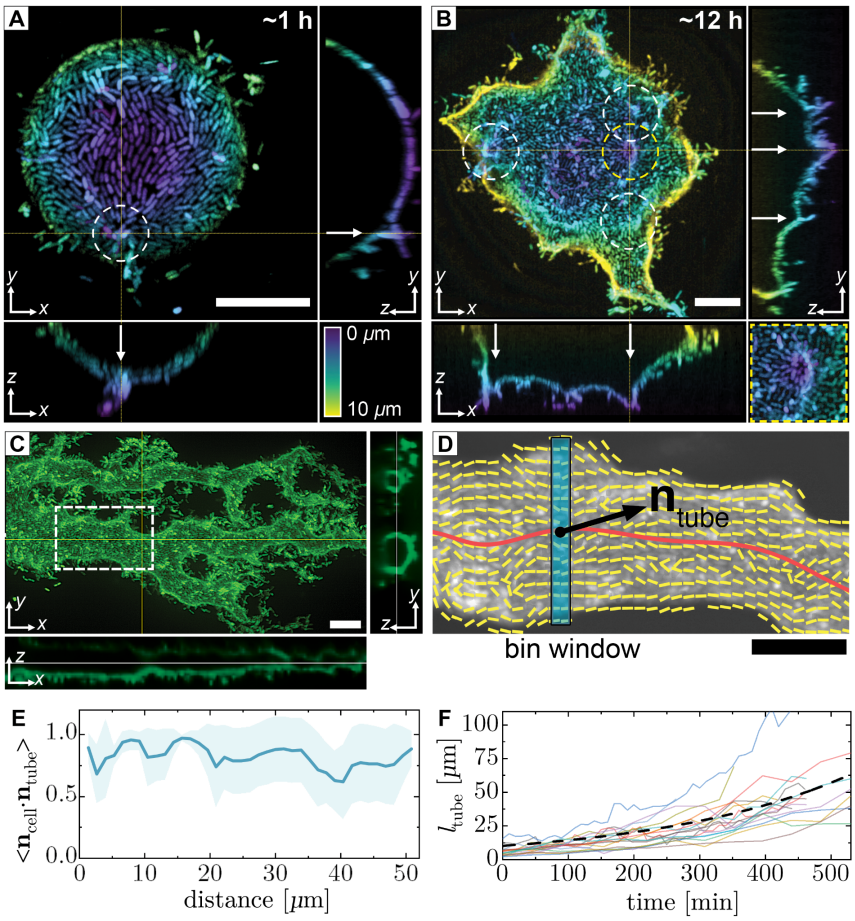

Fig. 2

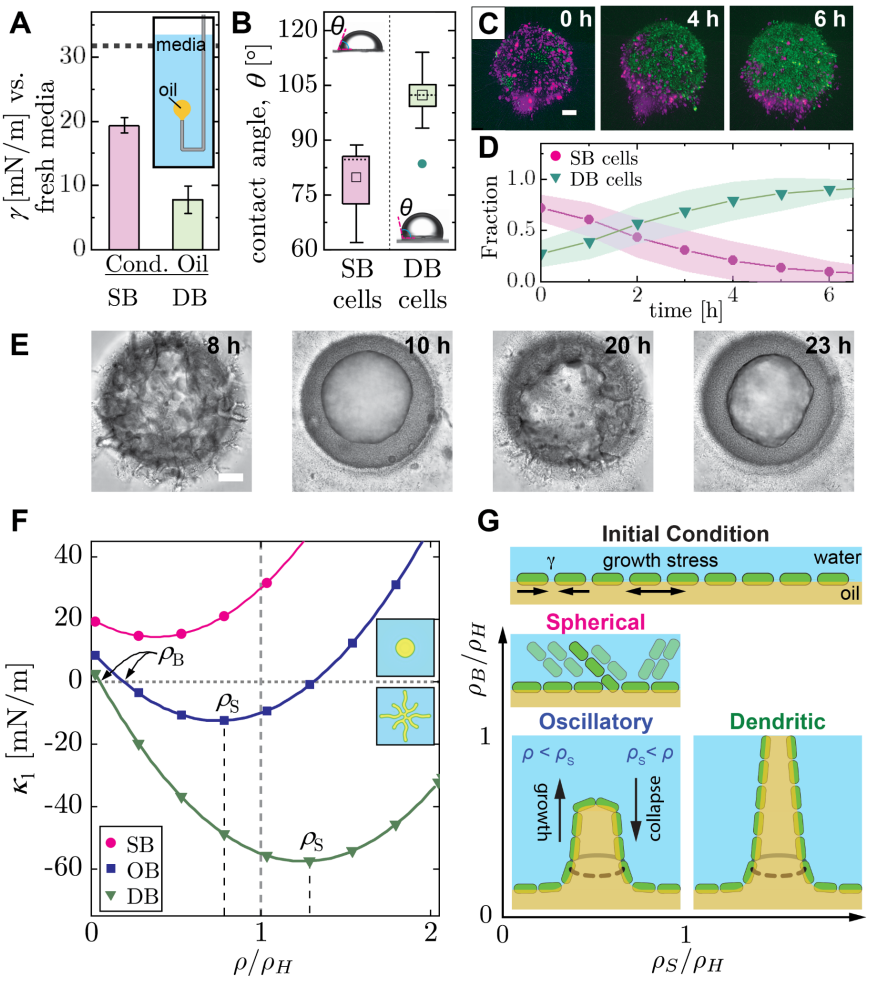

Fig. 3

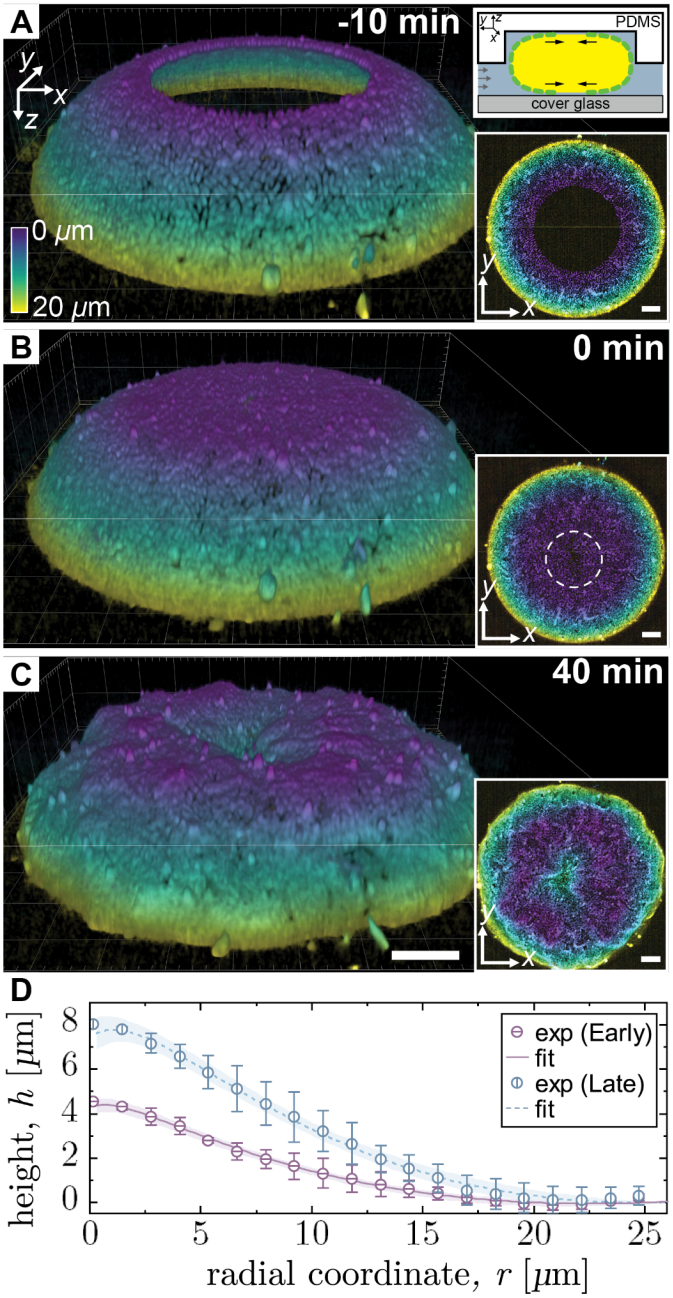

Fig. 4

FIGURE CAPTIONS

Fig. 1: Spherical and dendritic biofilm phenotypes on oil drops in a microfluidic trap. (A) Schematic of the microfluidic oil-drop trap device showing media-filled channels. Oil drops are trapped in the raised circular regions. Inlets on either side of the drop chamber connect to reservoirs that provide a gentle flow of media through the trap chamber. The white circles are pillars. Scale bar = 200 μm. (*center*) Schematic cross-section of an individual trap. (*right*) Bright-field image of a representative drop in a trap. The trap is outlined with a white dashed line, while the pocket is colored orange as a guide for the eye. Scale bar = 20 μm. (B) Representative time-lapse sequence of confocal images showing the development of the spherical biofilm (SB) phenotype. As the biofilm (green) grows the oil droplet (empty void) shrinks. Scale bar = 10 μm. (C) Maximum intensity projection confocal images showing the development of the dendritic biofilm (DB) phenotype on representative drops. Local nematic order is present at confluence (~0 h), buckling (0.1-0.5 h) and protrusions (2-4 h) appear later, and this is followed by large-scale remodeling of the interface leading to the formation of tubes (16 h). Scale bar = 10 μm. (D) Normalized surface area (S^*) of the oil as a function of time for (○) SB and (★) DBs. S^* for SBs is estimated from the measured normalized drop radius (R^*), shown in the inset. The dashed and dotted lines are best fits to S^* from our analytical models of oil degradation for SB and DB phenotypes, respectively. (E) Normalized oil volume (V^*) as a function of time estimated for data shown in (D). The dashed and dotted lines are best fits of our model (**Supplementary Information**) to the data. (inset) The S^*/V^* ratio as a function of time. The filled regions in (D,E) denote one standard deviation (±s.d.) (n_{SB} = 11 drops; n_{DB} = 12 drops). R, S, and V are normalized by their initial values, respectively. The filled symbols represent measurements, while open symbols are calculated.

Fig. 2: Dendrites originate from topological defects. Confocal images of representative droplets (A) early (~0 h) and (B) later (~12 h) in biofilm development. The images are color coded by depth. The dashed circles enclose topological defects with a charge of +1, while the arrows indicate protrusions. (B, inset) A magnified view of the central defect circled in yellow. (C) Confocal image of a bacteria-covered tube connected to a deformed droplet with corresponding orthogonal views (~20 h). (D) Director field of the visible cells in the dashed box in (C). The director field (yellow lines), tube axis (red line), the local tangent unit vector ($\mathbf{n}_{tube}$) along the tube axis, and the bin window (blue) are shown. (E) Axial order of the cells along the oil tube shown in (D). For a sliding window of width 1.5 μm along the tube, the local axial order is defined as the average of the individual scalar products between the director-field unit vectors ($\mathbf{n}_{cell}$) and local tangent unit vectors. $<\mathbf{n}_{cell} \cdot \mathbf{n}_{tube}> = 1$ for parallel alignment and 0 for perpendicular alignment. The shaded region represents ±s.d. (F) Oil tube length (l_{tube}) plotted as a function of time (n=18). The dashed line is a fit to the average tube length using an exponential equation (adjusted R-square = 0.96). All scale bars = 10 μm.

Fig. 3: Theoretical model of tubulation. (A) Interfacial tension (γ) between fresh media and SB- and DB-conditioned oil, respectively, measured using pendant drop tensiometry (n_{SB}=3; n_{DB}=10). The dashed line is the control value of γ for fresh medium and fresh oil ($n_{control}$=5). The conditioned oil was collected from SB and DB cultures (See **Methods**). (inset) Schematic of the tensiometry experiment. (B) Three-phase contact angles (θ) between a water drop deposited on a bacterial lawn, submerged in C16. The (□) is the mean, the horizontal dashed lines are the medians, and (●) represents an outlier (n_{SB}=10; n_{DB}=13). The *p*-value is 10^{-6} calculated with Welch's *t*-test. (inset) Images of the submerged water drops wetting the bacterial lawn. (C) Competition between SB cells (magenta) and DB cells (green) for interfacial area on a trapped droplet. DB cells displace a monolayer of SB cells over the course of ~6 h. (D) Measurement of the fractional coverage of SB and DB as a function of time from confocal images (n_{drops}=10). (E) Oscillatory behavior demonstrated by a culture sampled for duration the SB and DBs. (inset) Phase-field model confirms the prediction of the oscillatory biofilm (OB) phenotype (**SI**). (F) Model of the tension (κ_1 in the phase-field model) experienced by the tip of a tube as a function of normalized interfacial cell density (ρ/ρ_H) (see **Supplementary Materials** for details). We normalize cell density by the homeostatic interfacial cell density (ρ_H). Positive (negative) values of κ_1 indicate tube retraction (expansion). For the SB phenotype, tension is positive for all densities, thus tubes are unable to form. For the intermediate OB phenotype, the homeostatic density is located in a regime where the tension is increasing as a function of biofilm density. As cell density approaches ρ_H, this increasing tension further contributes to an increase in cell density, eventually triggering a collapse of tube structures. The slope at the y-intercept is k_1 = 3, 6, and 10 for the SB, OB, and DB models, respectively. ρ_B is the critical buckling density, where κ_1 crosses zero. κ_1 reaches a minimum at ρ_S, which is the optimal cell density beyond which the spontaneous curvature effect is reduced. (inset) Phase field simulation showing the SB phenotype for κ_1>0 and a tubulated droplet for κ_1<0. (G) Schematic phase diagram of the biofilm phenotypes in terms of normalized densities: ρ_S/ρ_H and ρ_B/ρ_H. Cell division drives an increase in cell density beyond ρ_S when ρ_S/ρ_H > 1, in which case oscillations the spherical and dendritic phenotypes occurs (OB); in contrast, stable dendrite (DB) occurs for ρ_S/ρ_H > 1.

Fig. 4: Defect mediated buckling of the surface of a confined droplet. (A-C) Time-lapse 3D confocal images of a 'flattened' drop, color coded by depth. (A) Prior to the formation of a cell monolayer, interfacial tension excludes cells from invading the flat circular regions at the top and bottom of the droplets, where they are in contact with the coverglass and PDMS ceiling. (upper inset) schematic of the flattened droplet; (lower inset): top view of droplet. (B) Confluent monolayer is formed at t_0 (see inset and **Fig. S10**). (inset) top view of droplet with a circle enclosing the nematic defects. (C) Dimple forms in the droplet at the defect. All scale bars = 10 μm. (D) Evolution of the dimple height (h) from xy-line profiles measured across the center of the drop shown in (C) at early (20 min) and late (26 ± 3 min) times, shown as a function of the radial coordinate (r). The fits to the data are based on **Eq. (2)**. The solid error bars and filled regions represent ±s.d on the experimental data and fits, respectively (see S8.2 in SI for more details on fitting procedure and error estimation). Early-profile data are the average of the x- and y-profiles (n=4) at t = 20 min, while the late-profile data are the average of the x- and y-profiles binned at 23, 26, and 29 min (n=12), respectively. To generate the dimensional values shown, we rescale the non-dimensionalized h-values by 4.5 μm and 8.0 μm at early and late times, respectively, while r is rescaled by 26 μm at all times.